Inventory of Supplemental Information

Figure S1. Coding instability in CA2 was not a result of cluster instability. Related to Figure 4.

Figure S2. Recording sites were confirmed to be located in CA2 using immunohistochemical and cytoarchitectural criteria. Related to Figure 1.

Figure S3. Examples of phase precession in individual CA2 place fields. Related to Figure 2.

Figure S4. Calculations and examples of shape-preference scores. Related to Figures 3 and 4.

Figure S5. Additional analysis of the similarity in hippocampal firing patterns over time. Related to Figure 4.

Figure S6. Changes in CA2 population activity over time were observed in individual animals. Related to Figure 4.

Figure S7. In the two-day single-shape paradigm, all three hippocampal subregions showed a moderate decorrelation within a recording block, but major differences between subregions emerged over longer recording intervals. Related to Figures 5 and 6.

Figure S8. Peak firing rates in place fields of multi-peaked CA2 cells were modulated independently. Related to Figure 4 and 7.

Table S1. Number of cells recorded from each animal in each experimental paradigm. Related to Figures 2-7.

Table S2. Descriptive statistics of the spiking properties of CA2 principal neurons during ten-minute random foraging sessions. Related to Figure 2.

Table S3. Full statistics for Mann-Whitney U tests that compare data between sessions. Related to Figures 3-7.

Supplemental Experimental Procedures
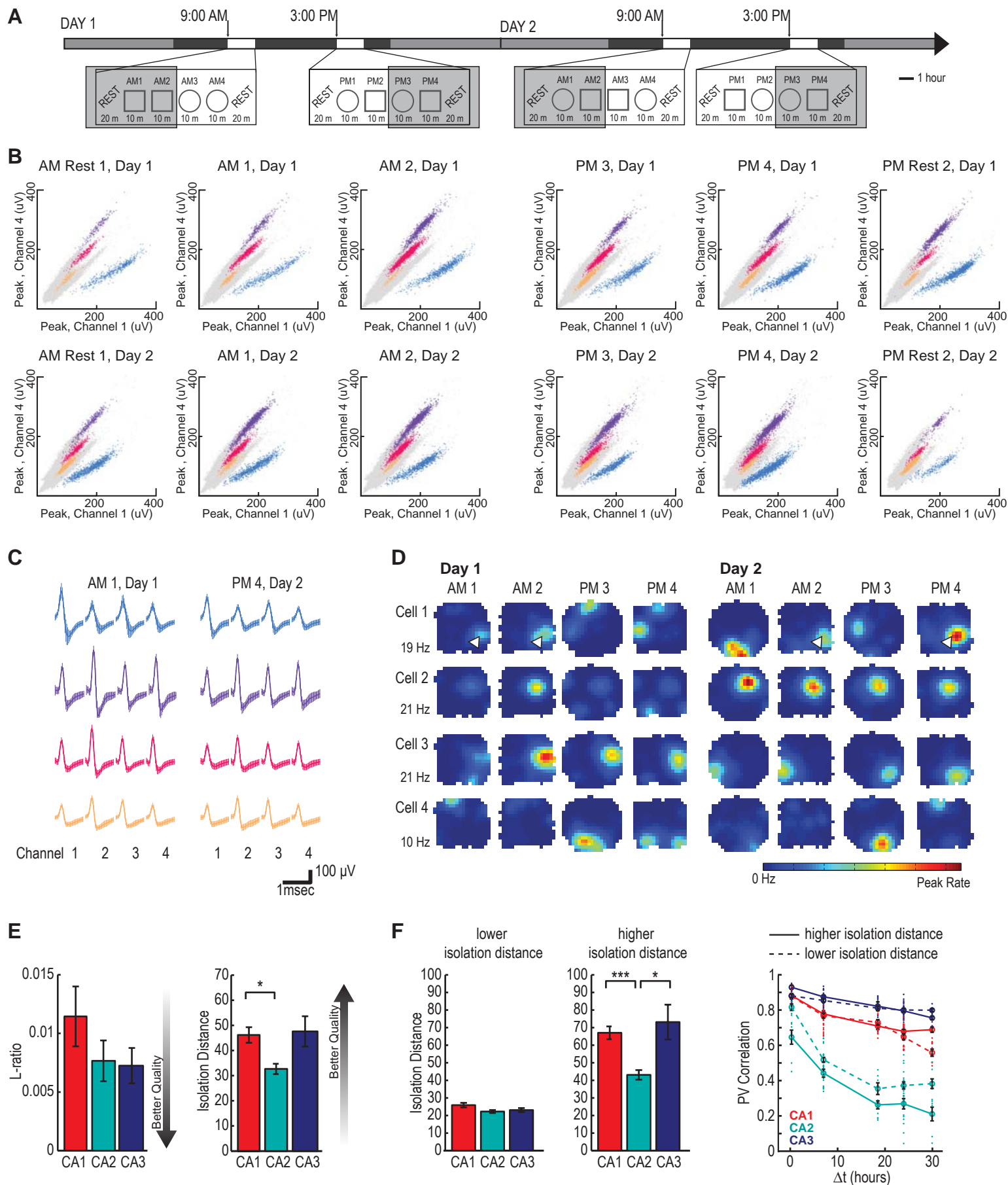
Supplemental References

Figure S1. Changes in CA2 activity are not a result of tetrode recording instability over time. (**A**) Complete experimental timeline. The gray boxes mark sessions that are highlighted in (B-D). (**B**) In each panel, the peak spike amplitude recorded on one channel of a tetrode is plotted against the peak spike amplitude recorded on another channel of the same tetrode. The same two tetrode channels are used for each plot, and different plots correspond to different time points in the experimental timeline as indicated by the gray boxes in (A). Each dot represents one sampled spike, and each dot color represents spikes that were assigned to a cluster. In amplitude plots, clusters are known to be generated by the regularity of the amplitude distribution of extracellular spikes from single cells. After defining clusters for all the recording sessions from one day, the cluster boundaries were applied to data recorded from the same tetrode on subsequent days. If clusters persisted in the same region of parameter space where they had been identified on the previous day, boundaries were adjusted to assure that all spikes that were determined to correspond to a cell were included within the boundaries. If the spikes for the set of clusters of a tetrode could be included with minor adjustments of the boundaries from the day before, the clusters were considered to correspond to the same set of cells as on the previous day, and the cells were included in analysis. Because we occasionally found that cells appeared to turn their spiking activity on or off during a subset of the recorded sessions, it was imperative to confirm that these effects were not simply a consequence of instability in the tetrode location. We thus only included cells in the analysis for which clusters could be identified within the same amplitude space at the beginning of the day (in the first sleep session or the first behavioral session in either shape) and at the end of the day (during the last sleep session or the last behavioral session in either shape). The cluster plots that are depicted correspond to cells 1-4 in **Figure 4B**. (**C**) Average waveforms from the clusters in (B). The color of the waveform matches the color of the corresponding spike cluster. The mean waveform (± standard deviation) is shown for the first behavioral session on the first day (left) and the last behavioral session on the second day (right). (**D**) Spatial maps from the same cells as in (B). The average firing rate in each 5×5 cm pixel is color-coded with a color scale from 0 Hz (blue) to the peak rate within the day (red). The peak firing rate for each cell is indicated to the left of the maps. Although spatial maps from tracked cells were not used to determine whether clusters were the same from one day to the next, we visually inspected spatial maps from tracked cells. In CA2, place fields frequently changed over the course of two days, but also reappeared at former locations after extended time intervals. For example, white arrowheads on the maps of Cell 1 indicate one location where a place field was often but not consistently present, including during the first and last behavioral session. This can be taken as further confirmation that the same cell was recorded across both days, even though a different spatial firing pattern appeared during intervening periods. (**E**) For each cell with more than 13 spikes per block, we measured cluster quality with two metrics: L-Ratio and isolation distance. Lower L-Ratios indicate better cluster quality, while higher isolation distances indicate better cluster quality. There was no statistical difference between regions for L-Ratio [Mann-Whitney U: CA1 (n=71 cells) vs. CA2 (n = 50 cells): $z = 0.67$, $P = 1$; CA1 vs. CA3 (49 cells): $z = 0.74$, $P = 1$; CA2 vs. CA3: $z = 0.13$, $P = 1$]. CA2 had moderately lower mean isolation distance compared to CA1 [Mann-Whitney U: CA1 (n=71 cells) vs. CA2 (n = 50 cells): $z = 2.54$, $P = 0.033$; CA1 vs. CA3 (n = 49 cells): $z = 1.09$, $P = 0.52$; CA2 vs. CA3: $z = -1.12$, $P = 0.52$]. (**F**) (Left) To confirm that differences in population coding between hippocampal subregions could not be attributed to differences in the isolation distance between spike clusters, we separated the cell sample into two groups based on whether each cell's isolation distance was greater than or less than the median isolation distance in that subregion (CA1, 40.6; CA2, 28.9; CA3, 34.5). There was no difference between regions when comparing the mean isolation distance for cell clusters in the lower isolation distance group [Mann-Whitney U: CA1 (n=36 cells) vs. CA2 (n=25 cells): $z = 1.49$, $P = 0.41$; CA1 vs. CA3 (n = 25 cells), $z = 1.40$, $P = 0.41$; CA2 vs. CA3: $z = -0.33$, $P = 0.74$], while CA2 had lower mean isolation distances than the other regions when comparing cells included in the higher isolation distance group [Mann-Whitney U: CA1 (n = 35 cells) vs. CA2 (n = 25 cells): $z = 4.53$, $P < 0.001$; CA1 vs. CA3 (n = 24 cells) $z = 1.10$, $P = 0.27$; CA2 vs. CA3: $z = -2.55$, $P = 0.022$]. These results indicate that CA2 clusters were not considerably less isolated than those in the other subregions, but rather that CA2 had fewer exceptionally well-separated clusters. (Right) Population vector correlations for the same box shape across time (as in **Figure 4C**) are plotted for cells from each group of cluster quality (high quality, connected by solid lines; lower quality, connected by dashed lines) for each region. The PV correlation declined to the greatest extent across time in CA2 regardless of whether we included only the cells with the lowest isolation distances or only the cells with the highest isolation distances [two-way ANOVA for lower isolation distance: brain region: $F(2) = 473.2$, $P < 0.001$; elapsed time: $F(4) = 107.2$, $P < 0.001$; interaction: $F(8) = 21.1$, $P < 0.001$; Tukey's HSD for all comparisons between regions, $P < 0.001$; two-way ANOVA for higher isolation distance: brain region: $F(2) = 631.4$, $P < 0.001$; elapsed time: $F(4) = 67.1$, $P < 0.001$; interaction: $F(8) = 6.9$, $P < 0.001$; Tukey's HSD for all comparisons between regions, $P < 0.001$]. Although the two curves for CA2 differ [two-way ANOVA: cluster quality group, $F(1) = 48.4$, $P < 0.001$; elapsed time, $F(4) = 78.1$, $P < 0.001$; interaction, $F(4) = 1.3$, $P = 0.28$], PV correlation values were lower in the higher isolation distance group than in the lower isolation distance group. Taken together, these findings indicate that the larger change in CA2 population activity over time could not be attributed to poorer cluster quality.

A

α-actinin-2 Immunohistochemistry + Cresyl Violet
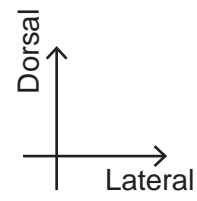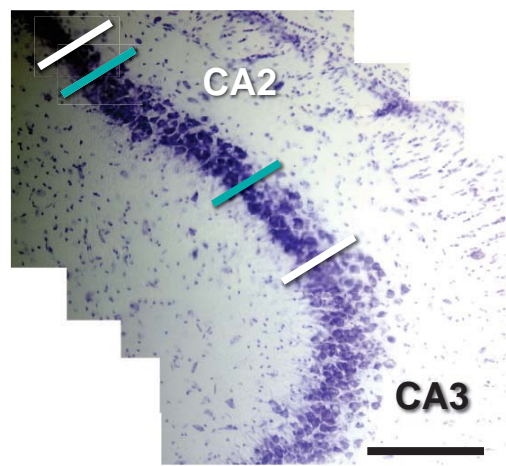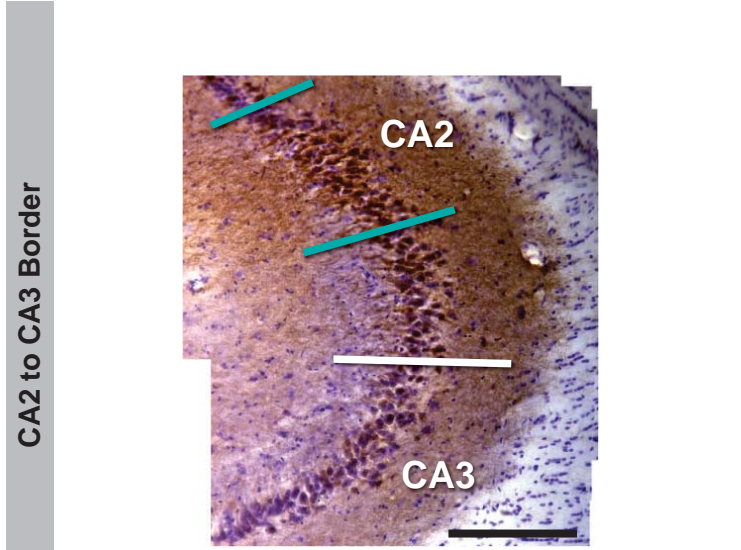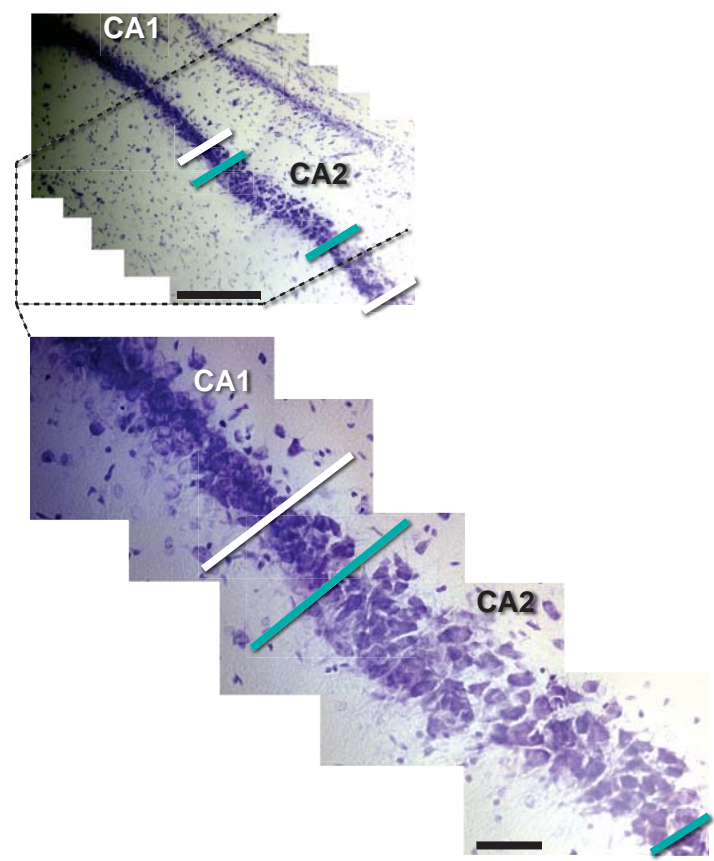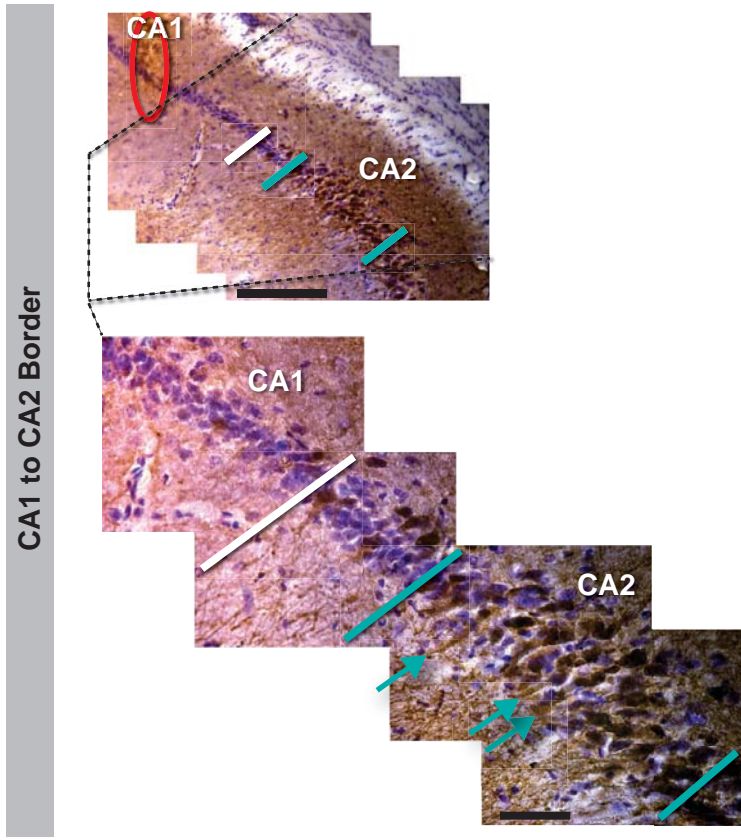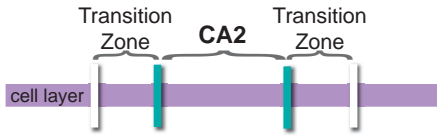RAT G:

B

Cresyl Violet
RAT C:

Figure S2. Confirmation of recording sites in each of the hippocampal subregions by using cytoarchitectural and immunohistochemical criteria. (**A**) Sections were immunostained for α-actinin-2 and counterstained with cresyl violet to compare the boundaries that were defined by each of the methods. Example images were taken along the hippocampal cell layer (20x, scale bar = 200 μm) and were stitched together throughout the region of interest to determine the boundaries between subregions (top: CA1 to CA2; bottom: CA2 to CA3). Through the region of interest delineated by dashed lines, additional images of the CA1 to CA2 cell border are shown at higher magnification (63x, scale bar = 50 μm). The CA2 area (demarcated by teal lines) was defined as the region with the most dense α-actinin-2 immunostaining (brown; see Wyszynski et al., 1998) of cell bodies and proximal dendrites (teal arrows). CA1 and CA3 (demarcated by white lines) were defined as the adjacent areas with weak immunolabeling. In addition, CA1 is characterized by smaller, densely packed cell bodies while CA3 shows larger cell bodies and a large fraction of cells outside of a densely packed inner sublayer. A transition zone between CA1 and CA2 (between the white and teal line) was defined as the area in which the cells were almost as densely packed as in CA1 and in which there was only sparse immunolabeling of cell bodies and dendrites. A transition zone between CA3 and CA2 (between the teal and white line) was defined as the area with larger cell bodies, but few cell bodies outside of the densely packed inner sublayer. (**B**) Cytoarchitectural criteria that matched the criteria from the α-actinin-2/cresyl violet co-staining were used in cresyl violet stained tissue to identify the hippocampal subregions and the transition zones. Only recordings from tetrode tracks (circled in color) that could be confidently assigned to a hippocampal subregion outside of transition zones were used in the analysis, and those in transition zones were excluded (see **Figure 1B** for the final recording locations of cells included in analysis).
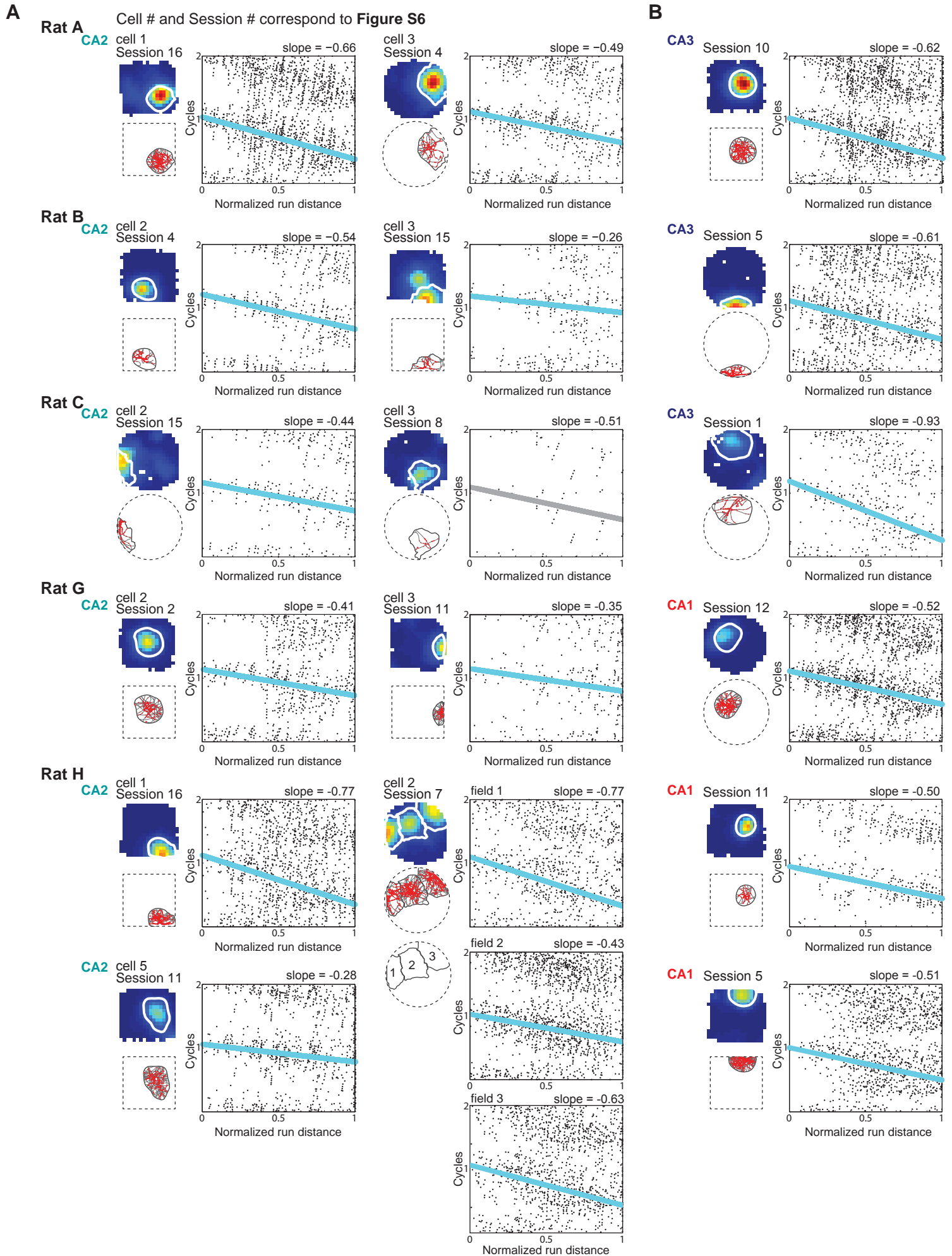
A

Rat A CA2

Cell # and Session # correspond to **Figure S6**

Rat B CA2

Rat C CA2

Rat G CA2

Rat H CA2

B

CA3

CA3

CA3

CA1

CA1

CA1

Figure S3. Examples of phase precession in CA2 place fields. (**A**) For each rat, the activity pattern is shown for 2-3 CA2 cells. (Upper left of each panel) Color-coded firing rate map (0 Hz, blue; peak rate, red) with the field boundary superimposed in white. The cell number and session number correspond to cell numbers and sessions numbers in **Figure S6**. (Lower left) Spikes within the place field (red dots) superimposed on the rat's trajectories through the field (gray lines). The field boundary is superimposed in black. (Right panel) Scatter plot of the normalized run distance against the theta phase at which each spike occurred. For better visualization, each spike is replotted in a second cycle with the beginning and end of each plotted cycle (0, 1, and 2) representing the trough of the theta cycle recorded in the hippocampal fissure. The regression line is superimposed in blue when the slope is significantly different from 0 ($P < 0.05$) and in gray when n.s., and its slope (in theta cycles/normalized run distance) is reported above each scatterplot. As common for the firing patterns of CA2 cells (**Figure 2**), Cell 2 from Rat H fired action potentials in multiple spatial locations within the environment. Phase precession was found in each of the three fields. Each regression line has a y-intercept between 1.0 and 1.1, which indicates that the phase precession cycle did not continue between fields but rather began at the boundary of each field. (**B**) For comparison, one example cell per rat is shown from either CA3 (rats A-C) or CA1 (rats G-H). Panels are arranged as described in A. Cell number is not indicated, as these cells do not correspond to those in other supplemental figures.
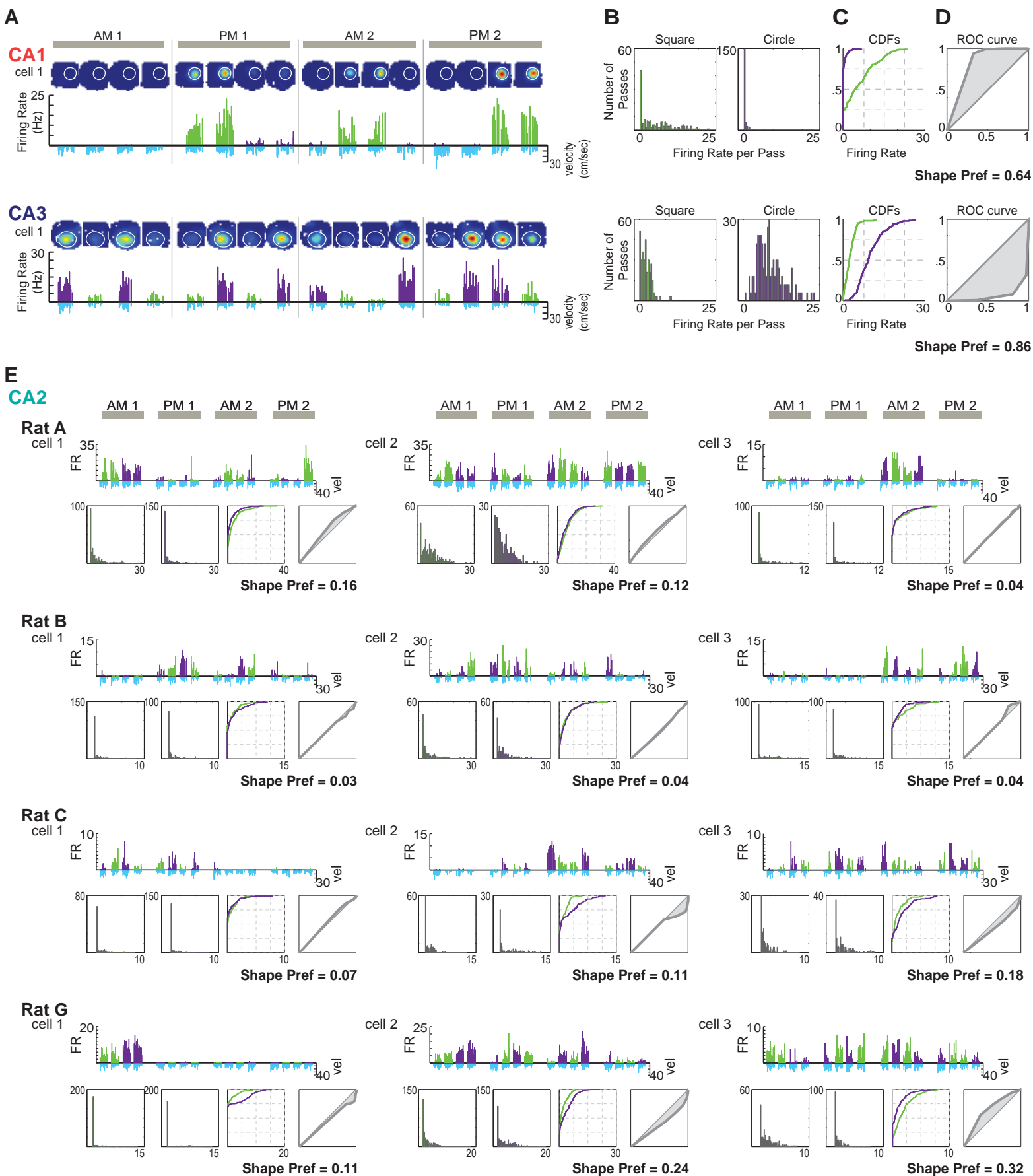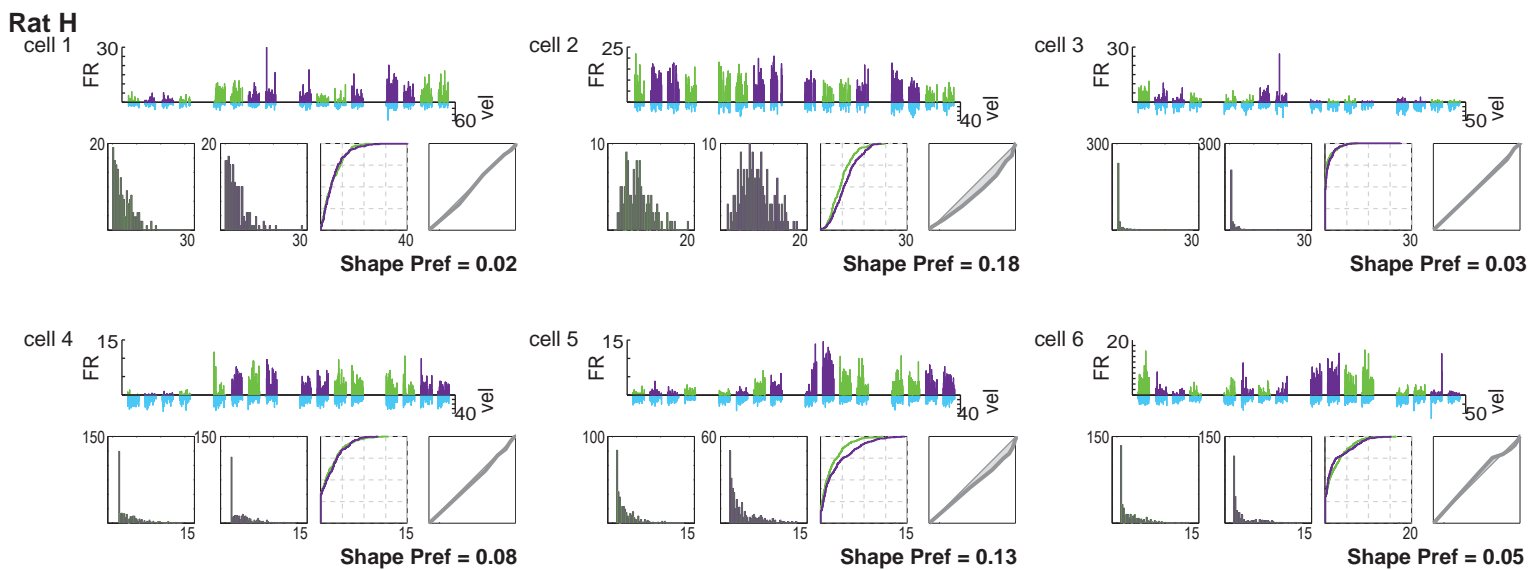
Figure S4. CA2 cells with low shape preference scores are found in all rats. (**A-D**) Calculation of shape-preference scores. (**A**) The activity pattern of two example cells (top, CA1; bottom, CA3) are shown for the 16 sessions of the two-day different-shape experiment. For each cell, color-coded firing rate maps (0 Hz, dark blue; peak rate, red) are shown for each 10-minute random foraging session, and the place field boundaries that were calculated from the average of the 16 spatial maps for each cell are superimposed in white. Below each rate map, the firing rate for each pass of the rat through the place field is shown in purple when the enclosure was in the circle configuration and in green when the enclosure was in the square configuration. The running velocity during each pass is plotted downwards in light blue. The presence of a velocity bar without a corresponding firing rate bar indicates passes without spikes. The CA1 cell was silent during the morning of the first day and became active in subsequent sessions, but only when the enclosure was shaped as a square. The CA3 cell exhibited higher firing rates in the circular shape than in the square shape throughout the entire recording sequence. Each cell demonstrated a clear firing rate preference for one of the box shapes, which resulted in a high shape preference score as described in B-D. (**B**) The firing rate distribution for passes through the place field when the box was in a square configuration (left, green) and for passes when the box was in a circle configuration (right, purple). The horizontal axes begin at -2 Hz in order to clearly visualize values at 0. (**C**) Cumulative distribution plots for the firing rates in B. Lines that are farther to the right indicate distributions in which higher rates were more frequent. (**D**) For each pair of firing rate distributions in C, the Receiver Operant Characteristic (ROC) curve was calculated (thick gray line) and the difference between the area under the ROC curve and area under the identity line was calculated (shaded in gray). This value was multiplied by 2, which results in a shape preference score that equals -1 for firing in only the circle, 1 for firing in only the square, and 0 for equal firing in the square and circle. The absolute value of the score measures the magnitude of the preference for either shape. The absolute shape preference score for the example cells is indicated in bold script. The same procedure was followed to calculate within-block absolute shape preference scores, except that only firing rates from sessions within a single block were used and that the scores for each of the four blocks were averaged. (**E**) Firing rate histograms, firing rate distributions, and shape preference scores for three CA2 place fields from each rat (A-G) and for six place fields from rat H. The firing rates correspond to those in the fields in **Figure S6** where the rate maps for all 16 sessions are depicted. The color scheme and layout of all plots is as described in A-D. Note that CA2 fields frequently have similar CDFs for each of the shapes, yielding shape preference scores close to 0.
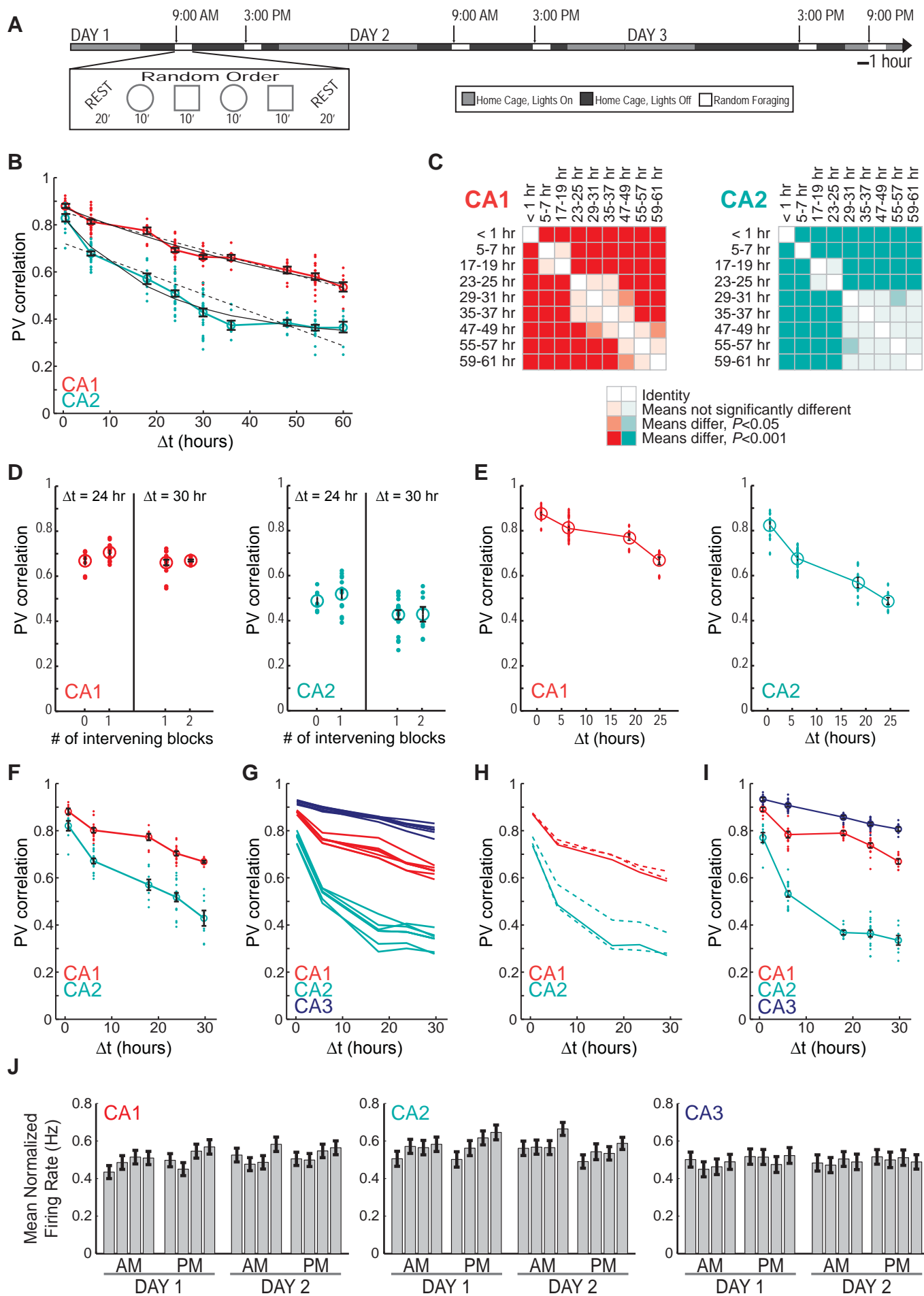
Figure S5. Additional analysis of the similarity in hippocampal firing patterns over time. (**A**) To confirm that an asymptote had been reached in CA2 after approximately one day, we extended hippocampal recordings across three days (see Supplemental Experimental Procedures). On the third day, all behavioral sessions were shifted by six hours, which makes comparisons for up to 60 hours possible for the population of cells that were tracked across all three days (n = 57 CA1 cells from 5 rats; n = 32 CA2 cells from 2 of 5 rats). (**B**) Population vector correlations between pairs of recordings in the same enclosure shape are shown as dots. Each dot corresponds to a pairwise comparison at the interval that is indicated on the horizontal axis. Symbols and error bars correspond to the mean +/- SEM for all comparisons at a particular time interval. Solid black lines represent best exponential fits to the data, and dotted black lines represent best linear fits. The explained variance was higher for the exponential compared to the linear fits in CA1 (R^2 exponential = 0.83, and R^2 linear = 0.81) and CA2 (R^2 exponential = 0.84, R^2 linear = 0.73). For the exponential fit, the time constant for the decay of the PV correlation is 76.3 hours in CA1 and 20.96 hours in CA2. (**C**) A two-way ANOVA on brain region and elapsed time revealed main effects of brain region [F(1) = 662.1, P < 0.001] and elapsed time [F(8) = 172.7, P < 0.001], as well as a significant interaction [F(8) = 9.97; P < 0.001] indicating that the way in which correlation changed with time varied between regions. For each region, a grid of Tukey's HSD comparisons is shown, and darker colors indicate more highly significant differences. Correlation levels in CA2 reached an asymptote by 30 hours. The slower change in CA1 compared to CA2 could be explained by proposing that CA1 integrates the continually changing signal from CA2 with a stable signal from CA3, which would presumably result in an intermediate level of place field stability in CA1 (see **Figure 8**). (**D-E**) Hippocampal CA2 and CA1 population patterns become decorrelated over time irrespective of intervening experience. To determine the possible role of intervening blocks on the population vector decorrelation, we analyzed hippocampal recordings on the third recording day. The 6-hour shift on the third day resulted in blocks between the second and third day that are separated by 24 hours without intervening behavioral testing and by 30 hours with one intervening block. (**D**) Population vector (PV) correlations for comparisons between recordings in the same enclosure shape at intervals of 24 hours or 30 hours (left, CA1; right, CA2). Each comparison between two sessions is shown as a dot, and the symbols and error bars are the mean +/- SEM for a time interval. Different numbers of intervening blocks did not result in differences in the degree of decorrelation [comparisons between 0 and 1 intervening blocks at the 24-hour interval: CA1, t(22) = -2.11, P = 0.094; CA2, t(22) = -1.07, P = 0.60; comparisons between 1 and 2 intervening block at the 30-hour intervals: CA1, t(22) = -0.49, P = 0.63; CA2, t(22) = -0.052, P = 0.96]. (**E**) PV correlations between pairs of recordings in the same enclosure shape. Only comparisons without intervening recording blocks are included. Each comparison between two sessions is shown as a dot, and the symbols and error bars are the mean +/- SEM for a time interval. A stronger decorrelation of CA2 population activity compared to CA1 population activity with time was also observed when there were no intervening recording blocks [Two-way ANOVA: brain region, F(1) = 203.0, P < 0.001; time difference, F(3) = 125.2, P < 0.001; interaction, F(3) = 10.9, P < 0.001]. (**F**) The population of neurons that were recorded in CA2 over three days reached asymptote after 30 hours (see B and C) compared to 18 hours in the larger dataset in **Figure 4C**. To test whether this was a result of including a behavioral session that was shifted by 6 hours on Day 3, we analyzed the same population of cells that was used for the analysis in (B) and (C) but only included comparisons for sessions that were recorded on Days 1 and 2. When comparing both data sets, the same level of decorrelation was reached at 30 hours. This result indicates that the variability in the time interval when asymptote was reached in CA2 was due to selecting a different set of animals for the analysis rather than due to selecting a different set of recording days for the analysis. (**G**) To further test the variability between individual animals in the two-day, two-shape condition (**Figure 4**), we performed a jackknife procedure in which PV correlations were calculated for sets of cells while leaving out one animal at a time. The mean correlation values for these reduced datasets are shown. In each case, there was a much more substantial decrease in coding similarity with time in CA2 compared to CA1 and CA3, although the decorrelation levels in CA2 after one day (18 to 30 hour intervals) varied from approximately 0.5 to 0.3. Despite the variability in the exact time course and decorrelation level, the full effect size in CA2 was reached within approximately one day (18-30 hrs) for all data sets. (**H**) Because one rat performed the experimental sequence twice with two different sets of independent cells, we also checked whether the observed results would differ substantially if the rat had been excluded (solid lines), or if the set of cells from one or the other repetition had been removed (dashed lines). In each case the decorrelation progressed much more rapidly in CA2 than in CA1, and reached a level between 0.3 and 0.4 in CA2 by 30 hours. (**I**) Finally, we only included CA1 and CA3 ensembles that were recorded simultaneously with CA2 ensembles in the analysis and found a pronounced difference in the rate of decorrelation between CA2 and each of the two other hippocampal subregions [Two-way ANOVA: brain region, F(2) = 1251.0, P < 0.001; time difference, F(4) = 167.3, P < 0.001, interaction, F(8) = 29.6, P < 0.001; Tukey's

HSD between brain regions, $P < 0.001$ for each comparison]. (**J**) Firing rates in CA2 did not show circadian fluctuations but varied with recording blocks. The mean +/- SEM of the normalized firing rate for all active CA1, CA2, and CA3 principal neurons is shown for each ten-minute recording session across the two-day, two-shape experiment. For each cell, the normalized firing rate was calculated by dividing the average firing rate for each session by that cell's average maximum firing rate throughout all 16 sessions. An ANOVA with day and session as factors did not reveal differences between Day 1 and Day 2 for any of the subregions, which is expected because the recording environments were already highly familiar on the first recording day [CA1: $F(1) = 1.56$, $P = 0.21$; CA2: $F(1) = 0.061$, $P = 0.80$; CA3: $F(1) = 0.035$, $P = 0.85$]. An effect of session identity was not found in CA3 [CA3: $F(7) = 0.36$, $P = 0.92$], was close to significance in CA1 [CA1: $F(7) = 1.97$, $P = 0.055$], and was found in CA2 [$F(7) = 2.41$, $P = 0.019$, Tukey's HSD revealed that the significant differences ($P < 0.05$) were between session 5 and sessions 4 and 8]. This result suggests that the effect was not circadian but that there were firing rate differences between the beginning and the end of recording blocks. An ANOVA with block and session within a block as factors confirmed that normalized firing rates did not vary between blocks in any region [CA1: $F(3) = 1.04$, $P = 0.37$; CA2: $F(3) = 1.53$, $P = 0.21$; CA3: $F(3) = 0.53$, $P = 0.65$] but varied within blocks in CA1 and CA2, but not CA3 [CA1: $F(3) = 3.82$, $P = 0.0097$; CA2: $F(3) = 5.23$, $P = 0.0014$; CA3: $F(3) = 0.21$; $P = 0.89$]. In CA1, sessions 1 and 2 had lower firing rates than session 4 (Tukey's HSD, $P < 0.05$), and in CA2 session 1 had lower rates than session 4 (Tukey's HSD, $P < 0.01$).
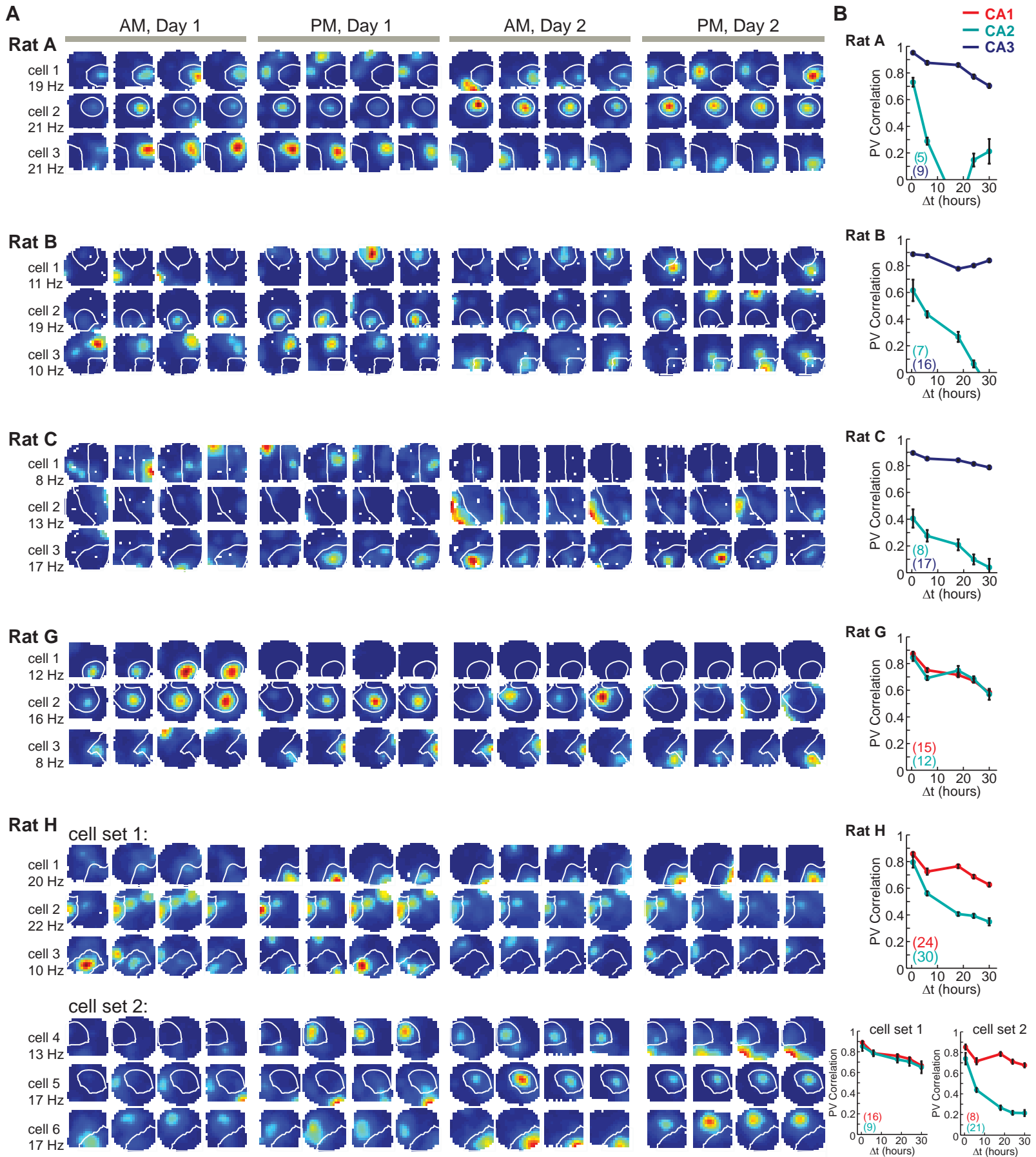
Figure S6. CA2 cells with profound changes in spatial firing patterns over time were found in each rat. (**A**) Three example CA2 cells are shown from each animal. (Each row) Color-coded firing rate maps of one cell that was recorded for 16 behavioral sessions throughout the course of the two day experiment. The color scale is from 0 Hz (blue) to peak rate within the entire testing sequence (red, indicated to the left) with pixels not visited in white. For each cell, the place field boundaries were computed on the average map of all 16 sessions in square and circular enclosures. The field boundary for one place field from each cell is highlighted in white. Rat H performed the experimental sequence twice with a unique set of cells during each repetition; cells 1-3 are from the first repetition and cells 4-6 are from the second repetition. (**B**) Mean population vector correlations (as described in **Figure 4C**) for simultaneously recorded cell ensembles from each rat. Pairs of recordings in the same enclosure shape at different time points were compared. The number of cells in the analysis is indicated at the lower left corner of each plot (in parentheses). Red, CA1; teal green, CA2; dark blue, CA3. Brain regions with fewer than 5 cells were not analyzed. The smallest difference between CA1 and CA2 in the population measure was observed in Rat G and cell set 1 of Rat H, nonetheless these recordings had clear examples of multiple cells that changed over time.
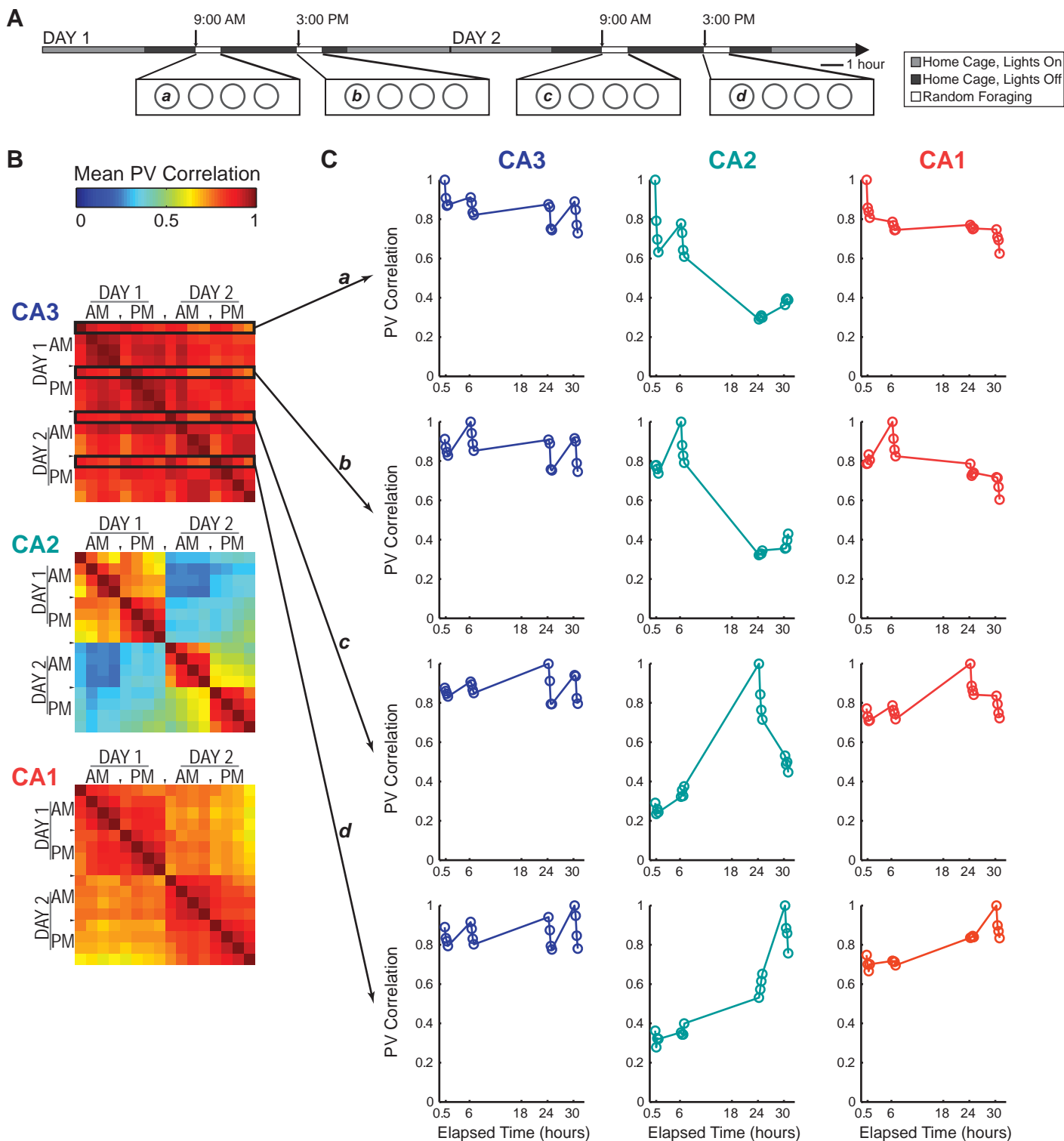
Figure S7. In the two-day, single-shape paradigm, all three hippocampal subregions show a moderate decorrelation within a recording block, but major differences between subregions emerge over longer time intervals. (**A**) In the timeline for the two-day single-shape experiment, the first 10-minute session of each AM or PM block is denoted with a lower case letter. (**B**) The complete correlation matrix for each hippocampal subregion is redrawn from **Figure 6D**. Correlation coefficients between sessions are represented on a color scale (0 to 1, dark blue to red). The pixel in the ith row and jth column in the correlation matrix represents the mean Population Vector (PV) correlation between the ith and jth sessions. Consequently, the matrix is symmetric with comparisons between the same sessions along the diagonal (their correlation coefficient is, by definition, 1).

The four rows that consist of comparisons with the first session of each block (a-d, see A) are highlighted on the CA3 matrix (black box). (**C**) PV correlations between the first session of each block (a-d) and all other sessions. Each hippocampal subregion is shown in a column (CA3, left; CA2, middle; CA1, right). The time axis represents elapsed time from the beginning of the experiment. In CA2, correlation falls off sharply in either direction from the reference point. In CA3, the PV correlations decrease within a block but reset at the beginning of each block. CA1 is intermediate between CA2 and CA3.

Figure S8. Peak firing rates in place fields of multi-peaked CA2 cells are modulated independently. (**A**) Five representative CA2 cells with multiple place fields are shown. For each cell, the place field boundaries were computed on the average map of all 16 sessions in square and circular enclosures. In the overview image on the left, the pl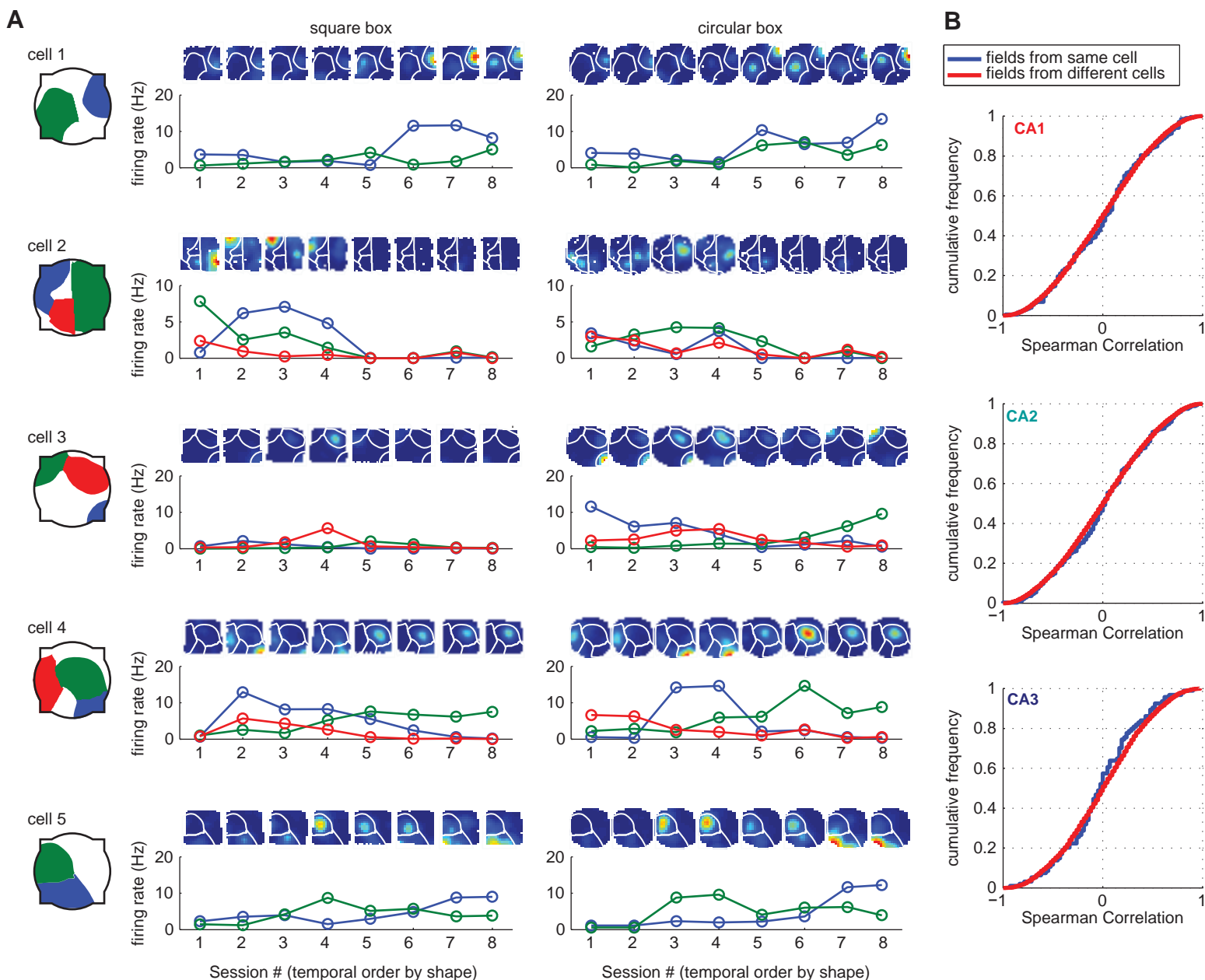ace field with the highest overall peak rate is shown in blue, the place field with the next highest rate is shown in green, and if present, a third place field is shown in red. To the right of the overview image, the firing rate maps of all 16 sessions over 2 days are depicted. Maps are ordered by time, but squares and circles are segregated into separate panels. Thus, sessions that are labeled 1-2 in the line graph were recorded on the morning of day 1, 3-4 were recorded on the afternoon of day 1, 5-6 were recorded on the morning of day 2, and 7-8 were recorded on the afternoon of day 2. For each cell, the peak rate of each place field in each behavioral session is plotted below the corresponding map. Line colors correspond to the place field depicted in the overview. (**B**) The set of 8 firing rates from a single field in each enclosure shape, ordered by time, constitutes a firing rate trajectory. For pairs of fields from the same cell, the Spearman correlation coefficient between firing rate trajectories was calculated. The same calculation was performed for pairs of fields from separate cells within the same subregion. To test whether firing rates in fields of single cells were modulated independently, we compared the distribution of correlation coefficients from within cell comparisons with the distribution of correlation coefficients from distinct cells. In all three CA regions, the distributions did not differ (Kolmogorov-Smirnov test: CA1, $K = 0.05$, $P = 0.76$; CA2, $K = 0.05$, $P = 0.50$; CA3, $K = 0.08$, $P = 0.54$). This indicates that the firing rates of individual place fields of the same cell are modulated as independently as firing fields from different cells.

	Two Shape			Single Shape			Third Day/Shift Day		
	CA1	CA2	CA3	CA1	CA2	CA3	CA1	CA2	CA3
Rat A	3	5	9	0	0	0	0	0	0
Rat B	0	7	16	0	0	0	0	0	0
Rat C	1	8	17	0	0	0	0	0	0
Rat D	30	0	10	0	0	0	17	0	8
Rat E	3	0	11	9	0	23	2	0	5
Rat F	13	0	8	16	0	47	11	0	5
Rat G	15	12	0	26	6	0	10	7	0
Rat H*	24 (16/8)	30 (9/21)	0	11 (5/6)	28 (6/22)	0	17 (9/8)	25(7/18)	0
Total	**89**	**62**	**71**	**62**	**34**	**70**	**57**	**32**	**18****

Table S1. Number of trackable cells per animal for each experimental condition. CA1 and CA3 data from rats A-F have been reported previously (Mankin et al., 2012). * Rat H performed the experimental sequence twice, separate sets of unique cells were recorded between the first and second set of experiments. The contribution of cells from each set of experiments is indicated in parentheses (first set/second set). ** Due to the small number of active CA3 place cells across the Third Day of experiments this data was not reported in the analysis.

Measure	N calculated on		Summary			Mann-Whitney Test					
			N	Mean	SEM		z-value	U	P	Adjusted P	Significance level
Mean firing rate (Hz)	Number of cells	CA1	89	0.53	0.048	CA1 vs CA2	-3.0	1977	0.0031	0.0062	P<0.01
		CA2	62	0.82	0.080	CA1 vs CA3	1.5	2720	0.13	0.13	n.s.
		CA3	71	0.52	0.078	CA2 vs CA3	3.4	1441	6.1 e-4	0.0018	P<0.01
Peak firing rate (Hz)	Number of cells	CA1	89	4.9	0.36	CA1 vs CA2	-0.30	2680	0.77	0.77	n.s.
		CA2	62	5.2	0.45	CA1 vs CA3	2.1	2551	0.037	0.087	n.s.
		CA3	71	4.2	0.53	CA2 vs CA3	2.2	1716	0.029	0.087	n.s.
Thresholded peak firing rate (Hz)	Number of cells with at least one session with peak rate > 2 Hz	CA1	76	7.5	0.34	CA1 vs CA2	0.85	1871	0.39	1	n.s.
		CA2	54	7.0	0.39	CA1 vs CA3	0.93	1712	0.35	1	n.s.
		CA3	50	7.4	0.58	CA2 vs CA3	0.22	1316	0.83	1	n.s.
Spatial information (bits/spike)	Number of cells	CA1	89	1.9	0.072	CA1 vs CA2	5.9	1211	4.8 e-9	1.4 e-8	P<0.001
		CA2	62	1.3	0.071	CA1 vs CA3	0.93	2888	0.35	0.35	n.s.
		CA3	71	1.8	0.080	CA2 vs CA3	-5.0	1102	7.2 e-7	1.4 e-6	P<0.001
Number of fields per cell	Number of cells	CA1	89	0.84	0.062	CA1 vs CA2	-2.4	2132	0.018	0.035	P<0.05
		CA2	62	1.1	0.096	CA1 vs CA3	2.3	2494	0.022	0.035	P<0.05
		CA3	71	0.68	0.082	CA2 vs CA3	3.7	1378	1.9 e-4	5.7 e-4	P<0.001
Number of fields per active cell	Number of cells with at least one field in at least one session	CA1	76	1.3	0.046	CA1 vs CA2	-2.8	1456	0.0044	0.0088	P<0.01
		CA2	54	1.5	0.071	CA1 vs CA3	1.5	1608	0.14	0.14	n.s.
		CA3	50	1.3	0.067	CA2 vs CA3	3.3	853	0.0011	0.0032	P<0.01
Field size (cm²)	Number of cells with at least one field in at least one session	CA1	76	803	49	CA1 vs CA2	-2.5	1515	0.011	0.034	P<0.05
		CA2	54	1000	64	CA1 vs CA3	0.38	1823	0.70	0.70	n.s.
		CA3	50	788	78	CA2 vs CA3	2.2	1008	0.026	0.053	n.s.
Field size (cm²), continuous half sessions	Number of cells with at least one field in at least one half-session	CA1	74	677	44	CA1 vs CA2	-2.3	1580	0.021	0.042	P<0.05
		CA2	56	839	56	CA1 vs CA3	1.9	1437	0.052	0.052	n.s.
		CA3	49	564	61	CA2 vs CA3	3.6	808	3.0 e-4	8.9 e-4	P<0.001
Fano factor of within-session firing rates per pass through field (Hz)	Number of place fields; analyzed in sessions with mean rate > 0.25 Hz	CA1	132	2.6	0.11	CA1 vs CA2	1.9	7590	0.057	0.11	n.s.
		CA2	133	2.3	0.093	CA1 vs CA3	2.8	3769	0.0044	0.013	P<0.05
		CA3	75	2.1	0.11	CA2 vs CA3	1.2	4488	0.23	0.23	n.s.
Within-session absolute change in firing rate	Number of place fields; analyzed in sessions with mean rate > 0.25 Hz	CA1	132	2.8	0.16	CA1 vs CA2	4.4	6033	1.1 e-5	0.3.3 e-5	P<0.001
		CA2	133	1.9	0.10	CA1 vs CA3	-0.76	4633	0.44	0.44	n.s.
		CA3	75	2.5	0.18	CA2 vs CA3	2.8	3803	0.0047	0.0093	P<0.01
Theta index	Number of cells with at least one session with more than 100 spikes	CA1	75	0.67	0.033	CA1 vs CA2	0.79	1858	0.43	0.85	n.s.
		CA2	54	0.66	0.050	CA1 vs CA3	1.3	1586	0.20	0.60	n.s.
		CA3	49	0.67	0.071	CA2 vs CA3	0.65	1224	0.52	0.85	n.s.
Intrinsic theta Frequency (Hz)	Number of cells with at least one session with more than 300 spikes	CA1	69	8.3	0.053	CA1 vs CA2	4.8	886	2.0 e-6	6.0 e-6	P<0.001
		CA2	52	7.7	0.10	CA1 vs CA3	4.6	567	5.3 e-6	1.1 e-5	P<0.001
		CA3	36	7.8	0.086	CA2 vs CA3	-0.36	892	0.72	0.72	n.s.
Phase-distance Slope (cycles/field)	Number of cells with at least one field with more than 100 spikes and a well-fit phase-distance line	CA1	68	-0.42	0.020	CA1 vs CA2	-5.0	851	6.8 e-7	2.1 e-6	P<0.001
		CA2	53	-0.27	0.023	CA1 vs CA3	-2.5	830	0.012	0.025	P<0.05
		CA3	35	-0.36	0.027	CA2 vs CA3	1.8	711	0.066	0.066	n.s.

Measure	N calculated on		Continuous Halves			Interleaved Halves			Continuous vs Interleaved			
			N	Mean	SEM	N	Mean	SEM	z-value	U	P	Significance level
Field size (cm²) for half sessions	Number of cells with at least one field in at least one half-session	CA1	74	677	44	77	624	36	0.38	2747	0.71	n.s.
		CA2	56	839	56	55	762	45	0.78	1408	0.44	n.s.
		CA3	49	564	61	52	602	54	-0.64	1179	0.52	n.s.

Table S2. Descriptive statistics for the spiking properties of CA1, CA2, and CA3 neurons during 10-minute random foraging sessions. All reported statistics were first calculated for each of the sixteen 10-minute sessions (see **Figure 1D**) and were then averaged across sessions to yield a single value per cell or per field. For measures reported in the larger table, comparisons between regions were performed using a Mann-Whitney U Test. The Holm-Bonferroni correction for multiple comparisons was applied to obtain adjusted P values. The measure reported in the smaller table compares two methods of calculating field size, and comparisons were performed within each region using a Mann-Whitney U Test.

Measure	N calculated on		Summary			Mann-Whitney U Test					
			N	Mean	SEM		z-value	U	P	Adjusted P	Significance level
Shape preference (within single block)	Place fields with at least 5 passes through the field in each of the 16 sessions	CA1	105	0.50	0.023	CA1 vs CA2	7.6	2372	3.2E-14	9.7E-14	P < 0.001
		CA2	112	0.27	0.016	CA1 vs CA3	0.62	2312	0.54	0.54	n.s.
		CA3	47	0.49	0.041	CA2 vs CA3	-4.5	1432	6.0E-06	1.2E-05	P < 0.001
PV corr at lag 1 (same box shape)	Comparisons between population vectors with at least 25 cells	CA1	7	0.90	0.0087	CA1 vs CA2		4	0.030	0.091	n.s.
		CA2	5	0.85	0.014	CA1 vs CA3		26	0.87	0.87	n.s.
		CA3	8	0.87	0.031	CA2 vs CA3		13	0.35	0.71	n.s.
PV corr at lag 2 (same box shape)	Comparisons between population vectors with at least 25 cells	CA1	6	0.85	0.019	CA1 vs CA2		1	0.019	0.038	P < 0.05
		CA2	4	0.67	0.052	CA1 vs CA3		0	0.010	0.029	P < 0.05
		CA3	4	0.92	0.011	CA2 vs CA3		0	0.029	0.038	P < 0.05
Shape preference (across two days)	Place fields with at least 5 passes through the field in each of the 16 sessions	CA1	105	0.43	0.026	CA1 vs CA2	8.2	2106	3.2E-16	9.3E-16	P < 0.001
		CA2	112	0.15	0.015	CA1 vs CA3	-0.23	2409	0.82	0.82	n.s.
		CA3	47	0.44	0.043	CA2 vs CA3	-6.1	1017	1.1E-09	2.2E-09	P < 0.001
Area covered by spatial drift of place field center	Place fields in the single-shape paradigm that were active in at least 3 sessions	CA1	51	95	16	CA1 vs CA2	-4.7	743	3.3E-06	9.8E-06	P < 0.001
		CA2	61	350	47	CA1 vs CA3	1.8	475	0.073	0.073	n.s.
		CA3	25	57	15	CA2 vs CA3	4.5	278	5.4E-06	1.1E-05	P < 0.001

Measure	N calculated on		Same Box Shape			Different Box Shape			Same vs Different		
			N	Mean	SEM	N	Mean	SEM	z-value	U	P	Significance level
PV correlation at lag 2	Comparisons between population vectors with at least 25 cells	CA1	6	0.85	0.019	10	0.43	0.030		0	2.5 e-4	P < 0.001
		CA2	4	0.67	0.052	8	0.58	0.039		10	0.37	n.s.
		CA3	4	0.92	0.011	8	0.55	0.054		0	0.0040	P < 0.001

Table S3. Full statistics for all comparisons using a Mann-Whitney *U* Test in analysis over time scales longer than 10 minutes. The first segment of the table reports comparisons between regions. The Holm-Bonferroni correction for multiple comparisons was applied to obtain adjusted *P* values. The second portion of the table compares PV correlations at Lag 2 between sessions recorded in the same box shape and sessions recorded in different box shapes; comparisons were performed within each region. Gray boxes indicate tests for which the sample size was too small to calculate a z-value.

Supplemental Experimental Procedures

Subjects and surgeries. CA2 data were collected from five male, experimentally naïve, Long Evans rats with a preoperative weight of 400-510 g. Animals were housed individually and maintained on a 12-h light/12-h dark schedule with lights off at 6:00 am. All behavioral testing occurred in the dark, except when noted. The data from three of the five animals were recorded simultaneously with previously reported CA1 and CA3 recordings (Mankin et al., 2012). For comparisons of the CA2 data with all available CA1 and CA3 recordings from the same experimental design, previously published data from three additional animals without CA2 recordings were also included (Mankin et al., 2012).

All experimental procedures were performed as approved by the Institutional Animal Care and Use Committee at the University of California, San Diego and according to National Institutes of Health and institutional guidelines. At the time of surgery, rats were anesthetized with isoflurane (2-2.5 % in O_2) and buprenorphine was administered as an analgesic. An electrode assembly consisting of fourteen independently movable tetrodes was implanted above the right hippocampus (AP 3.9-4.0 mm posterior to bregma, ML 3.0-3.5 mm). Tetrodes were prepared as described previously (Leutgeb et al., 2007) and were advanced to the hippocampal cell layer using techniques optimized for recording stability across time (Mankin et al., 2012).

Behavioral Procedures. After one week of recovery from surgery, rats were partially food-deprived and trained to forage for randomly scattered cereal crumbs in an enclosure with walls that could be shaped either as a square (80 cm by 80 cm) or as a 16-sided polygon (50 cm radius; referred to as 'circular enclosure'). A polarizing white cue card (20 cm wide) was placed on an inside wall of the enclosure. The center of the enclosure was always located at the same place in the room, and the angle of the cue card compared to external room cues was kept constant. Training was performed in two daily blocks. For all rats, the first block started between 8:30 and 10:00 am and the second block between 2:30 and 4:00 pm. For

each individual rat, the daily start time of each block varied by less than 30 minutes. Rats were returned to the animal housing room between the morning and afternoon training blocks.

Rats were trained to run for four 10-minute sessions during each block, with two sessions in the square enclosure and two sessions in the circular enclosure. The order of the shapes was varied randomly within each training block. The rats were allowed to rest for five minutes between sessions, and training blocks were flanked by 20 minute sleep sessions. The floor of the enclosure was cleaned with water between each session. Following the sleep session at the end of the afternoon training block, rats were screened for single-unit activity. One tetrode remained in the cortex and was used as a reference for all recordings. Another tetrode was lowered to the hippocampal fissure to record hippocampal local field potentials. The remaining twelve tetrodes were slowly advanced towards the hippocampal cell layer. Prior to the implantation of the recording array, the relative spatial arrangement of all tetrodes with respect to each other was noted. This allowed for the targeting of more anterolateral tetrodes towards CA2/CA3 and the more posteromedial tetrodes towards CA1/CA2. The placement of all tetrode recording sites in each of the hippocampal subregions was determined from histological material that was prepared as described below.

Electrophysiological recordings throughout the morning and afternoon sessions were initiated when multiple well-isolated cells ($> 300\ \mu V$) were observed on most tetrodes. The recording phase of the experiment began after 9 to 20 days of behavioral training. Recordings were first conducted for 2 days in the standard training paradigm that included recordings in the square and circular enclosure (referred to as two-shape, day 1; two-shape, day 2). In five animals (two with CA2 recordings), recordings were also performed on a third day that was identical to the first two recording days, except that the start times of the blocks were shifted by 6 hours, so that the first block occurred at 3:00 PM and the second at 9:00 PM. The second block was thus during the light phase of the light/dark cycle (**Figure S5**). Additionally, four animals (two with CA2 recordings) performed two days of behavior in which all sixteen random foraging sessions were conducted in a single enclosure shape (single-shape, day 1; single-shape, day 2). For each

animal, we selected the shape in which we identified the larger number of active cells during the recording on the preceding day. This paradigm was otherwise identical to the two-shape paradigm. In one animal, the five-day recording sequence that included the three days in the two-shape paradigm and the two days in the single-shape paradigm was repeated once. In this animal, the first set of recordings began after 16 days of training and the second set began after 22 days of training, and the set of recorded cells during each sequence were from different tetrodes or, when from the same tetrode, determined to be unique by inspecting the clusters. Therefore, the cells that were recorded during each repetition were included as separate cells in the analysis.

Recording procedures. For recording spikes and local field potentials, the electrode assembly was connected to a multichannel head-mounted preamplifier. The *x-y* position of light emitting diodes on the preamplifier was tracked at 30 Hz by processing video images. Unit activity was amplified and band-pass filtered at 600 Hz to 6 kHz. Spike waveforms above a trigger threshold (40-60 µV) were time-stamped and recorded at 32 kHz for 1 ms.

Cell-tracking and single unit isolation. Because our study depended on being able to follow the same set of principal cells over an extended time period, we developed a customized version of MClust (A. D. Redish, A.D. MClust. http://redishlab.neuroscience.umn.edu/MClust/MClust.html) with added functions that allowed for the comparison of the cluster boundaries of each cell throughout a series of rest and 10-minute recording sessions. Clusters that persisted in the same region of parameter space throughout two days were accepted as single cells for further analysis. Rest sessions at the beginning and end of each behavioral session were analyzed to confirm that changes in cell activity patterns in behavior were not a result of tetrode instability. Care was taken to accept only cells that could be precisely followed from the beginning to the end of the data analysis, and all clusters were inspected visually to ensure that rate changes that were observed could not be attributed to clusters drifting outside of defined cluster boundaries (**Figure S1**).

Postmortem confirmation of recording location. Rats received an overdose of sodium pentobarbital and were perfused transcardially with saline and either 4 % formaldehyde or, when immunohistochemistry was performed, 4 % paraformaldehyde. The brains were extracted and stored in the fixative with 30 % sucrose. Frozen coronal sections (40 μm) were cut, and each section through the part of the hippocampus with electrode tracks was collected and stained with cresyl violet. To confirm our delineation of CA field boundaries, immunohistochemistry using antibodies against α-actinin-2 was performed as previously described (Ratzliff and Soltesz, 2001) on tissue from two recording animals and two additional animals in which recording was not performed. Immunoreactivity for α-actinin-2 has been shown to be high in CA2, in the molecular layer of the dentate gyrus, and in the cell bodies of interneurons scattered throughout the hippocampus (Wyszynski et al., 1998). Free-floating sections were incubated with mouse anti α-actinin-2 antibody (1:50,000; clone EA-53, Sigma) overnight at 4°C. On the following day, the sections were incubated for 2 hours with HRP-conjugated horse anti-mouse secondary antibody (1:1,000; Sigma). The secondary antibody was visualized by reaction with diaminobenzidine, and sections were counterstained with cresyl violet.

The final tetrode positions were determined by three-dimensional reconstruction of the tetrode array in serial sections. Because the brain was cut at a small angle compared to the orientation of the electrode tracks, the path of each electrode through the brain could be visualized as elongated segments of tissue damage in each section. The tip of each electrode was found by tracking the damage throughout the series of sections that was arranged from anterior to posterior (see Figure S1 in Leutgeb et al., 2007 for the appearance of the tracks in serial sections). Tetrodes were not moved after electrophysiological recordings, and recordings from a tetrode were included in the data analysis if the tetrode's deepest position was in or just below the pyramidal cell layer of CA1, CA2, or CA3. In tissue for which immunohistochemistry was performed, CA2 was defined as the region with dense α-actinin-2 staining in cell bodies and proximal dendrites. We confirmed that this definition coincided with morphological criteria, so that the boundaries of CA2 could also be identified in tissue in which we did not stain for α-

actinin-2. The boundary between CA1 and CA2 was drawn at the transition where the cell layer thickens and where cell bodies increase in size and become less densely packed (Lorente de No, 1934; Woodhams et al., 1993). The boundary between CA2 and CA3 was drawn at the transition where the cell layer becomes less compact and where large cell bodies are scattered outside the continuous cell layer (**Figure S2**).

To further increase confidence that tetrodes were correctly assigned, we excluded tetrodes that were at transitions between CA regions. The transition zone between CA1 and CA2 was defined as the area in which there was only a minor decrease in packing density compared to CA1. This zone corresponded to an area in which the immunolabeling of cell bodies and dendrites was sparse in the α-actinin-2 stained section. The transition zone between CA3 and CA2 was defined as the area with larger cell bodies, but with few cell bodies outside of the densely packed inner sublayer. Because the CA2/CA3 border shows a more gradual transition than the CA1/CA2 border, we obtained further confirmation of tetrode assignment to CA2 by measuring the distance of all CA2 tetrodes from the CA1/CA2 border. At the anteroposterior level where the majority of recording tetrodes was located, the proximal to distal extent of the principal cell layer within the CA2 region, as defined by α-actinin-2 staining in proximal dendrites, ranged from approximately 350 μm to 425 μm. All tetrodes assigned to the CA2 region were less than 350 μm from the CA1/CA2 border. We also confirmed that tetrodes that were assigned to CA3 were well beyond the CA2/CA3 border, and the nearest tetrode was at a distance of more than 700 μm.

Spatial tuning and correlation. For each well-isolated neuron, a spatial firing rate distribution was constructed in the standard manner, by summing the total number of spikes that occurred in a given location bin (5 cm by 5 cm), dividing by the amount of time that the animal spent in that location, and smoothing with a Gaussian centered on each bin (Leutgeb et al., 2007). Spatial information per spike was calculated for each spatial firing rate map as $I = \sum_i P_i \frac{R_i}{R} log_2 \frac{R_i}{R}$, where i indexes the spatial bins, P_i is the

probability of occupancy in each bin, R_i is the mean firing rate in each bin, and R is the mean firing rate across the spatial map (Skaggs et al., 1993).

Place field boundaries, size, number, and stability. Place field boundaries for each cell were calculated as described previously (Mankin et al., 2012) by using maps from either single sessions or the average of 4, 8, or 16 recording sessions. Field boundaries from single sessions were used for the initial analysis to avoid bias that could result from drifting fields (**Figure 2** and **Table S2**), and field boundaries from averages across sessions were subsequently used to allow for comparisons over different time intervals. To consider whether short-term spatial drift accounted for differences in field sizes between regions, boundaries were also defined on maps created from 5 minutes of data that were either sampled continuously (the first or second half of each session) or in an interleaved manner (using either the even or the odd minutes of each session). To ensure that broad firing fields were not excluded from the analysis, we used a low threshold and included all fields with peak firing rates of greater than 2 Hz in a single session. Because this criterion was not stringent, we obtained higher proportions of active cells (59.2 % in CA1, 68.2 % in CA2, and 48.1 % in CA3) than typically reported for CA1 and CA3 in similar recording environments (Leutgeb et al., 2004). To confirm that there was also a higher proportion of active cells in CA2 with a more stringent criterion, we determined the proportion of active cells with peak rates greater than 5 Hz, which resulted in 41.6 % active cells in CA1, 45.8 % active cells in CA2, and 29.5 % active cells in CA3. These values are comparable to those that are typical and confirm that CA2 has more active cells than the other CA subregions irrespective of a particular threshold. In all analysis that averaged maps from recordings in square and in circular shapes, fields with peak firing rates that exceeded 1 Hz were included. The lower threshold for analysis that included the two shapes was used to correct for the fact that fields that were active in only one of the two box shapes would yield a reduced average firing rate in average maps that also include the box shape in which the cell was silent.

After defining field boundaries, the area within the field boundary was taken as the size of the place field, and the bin with the peak firing rate was taken as the field center. For each field that was active in at least three sessions, the area of the convex hull traced out by the field center was used as an estimate for the spatial stability between recording sessions. For each place field, a 'pass' through the field was defined as a trajectory through the place field that included a section through the area of the field in which the firing rate was > 50 % of the maximum firing rate. The mean rate per pass was taken as the number of spikes during the pass divided by the duration of the pass. To estimate the variability of the firing rates, the Fano factor per field was calculated as the variance in firing rate per pass divided by the mean firing rate. Additionally, the change in firing rate throughout a recording session was estimated by calculating the regression for predicting the firing rate from the elapsed time within the session. The absolute value of the slope of the regression line was taken as the change in firing rate over time, and a slope of 0 indicated that there was no increase or decrease in rate. To avoid that the results reflect variability of cells with very low firing rates or very few passes, sessions during which the mean rate per pass in a field was < 0.25 Hz or during which there were fewer than 5 passes were excluded from the analysis of the Fano factor and the within-session change in firing rate.

Theta index and intrinsic frequency. For each cell and each 10-minute session, we calculated the spike autocorrelogram using a time bin size of 2 ms. For the range between -500 ms and 500 ms, each autocorrelogram was fit with the following equation

$$y(t) = [a(\cos(\omega t) + 1) + b]e^{-|t|/\tau_1} + ce^{-t^2/\tau_2^2},$$

where t is the time lag, y is the correlation coefficient at that time lag, and a, b, c, τ_1, τ_2, and ω are the fit parameters. The theta index was defined as the ratio a/b (Royer et al., 2010). We also calculated the spectrum of the autocorrelogram using the multi-taper method (http://chronux.org) (Mitra and Bokil,

2008) and defined the intrinsic theta frequency for each cell as the frequency within the 4-11 Hz range with the largest power.

LFP, phase of firing, and phase precession. A local field potential (LFP) was recorded from the hippocampal fissure of each animal and then band-pass filtered in the theta range (4-12 Hz). A Hilbert transform was performed on the theta signal to decompose it into theta phase and amplitude. Periods when theta amplitude fell below two standard deviations of the mean theta amplitude were designated as low-theta-power periods and were not included in the analysis. For each identified firing field in a 10-minute session, the theta phase for each spike within the field was calculated. To analyze phase precession, all spikes from all passes through a field were pooled. For fields with at least 100 spikes, a best-fit line between phase and distance traveled within the place field was found using the circular-linear fit method (Kempter et al., 2012). The method is iterative, and fields for which the fit did not converge (CA1: 2.75%, CA2: 3.22%, CA3: 1.18%) were excluded from the analysis. The median slope of all fitted fields was compared to zero using the sign test for medians.

Single-Session Firing Properties. To characterize single-session firing properties and compare them between CA regions, we calculated the average firing rate, the spatial information, the number of fields, the theta index, and the intrinsic theta frequency for each cell in each of the 16 sessions recorded across two days. In addition, each cell's firing fields were defined in each session, and the peak rate and field size of each field were measured. If multiple fields were identified, the peak firing rate and field size of all fields within a session were averaged. The statistics for each CA region were calculated after averaging the values for each cell over the 16 recording sessions, and one value per cell was thus used for statistical analysis. To quantify the variability of firing within a field, we calculated the Fano factor for the firing rates during individual passes through the field within each session, and we calculated the slope of the regression line between the firing rate per pass and time when the pass occurred within each recording session. For these calculations, place field boundaries were defined using the average firing map of all 16 behavioral sessions,

and the statistics for each CA region were calculated after averaging the values for each field over the 16 recording sessions. Hippocampal CA regions were compared using the Mann-Whitney U test, and the conversion of the U value to the z statistic is reported if the number of observations in each group was greater than 20. If the number of observations was smaller, the conversion to the z statistic is not accurate and the U value is reported in the text. Significance levels were corrected for multiple comparisons by applying the Holm-Bonferroni correction. To find the proportion of active cells, a cell was considered active in a session if its maximum firing rate in any spatial bin exceeded a threshold (2 Hz). The proportion of active cells in each region was calculated for each session and then averaged across the 16 sessions.

Shape Preference. A shape preference score was calculated for each firing field by measuring the degree to which the distribution of firing rates in one shape was separated from the distribution of firing rates in the other, as previously described (Mankin et al., 2012). Briefly, for every pass through a place field, the average firing rate was computed, and the rates from all passes in each box shape were pooled across either a single block across 16 sessions to yield the firing rate distributions in the square and in the circular enclosure for that place field. The Receiver Operant Characteristic (ROC) curve was computed for these distributions. The area under the ROC curve may take values between 0 and 1 and can be used as a measure of the overlap of two distributions. We scaled this score by subtracting 0.5 to center it at zero and by multiplying it by 2 so that its range was between -1 and 1. We then took the absolute value so that equal firing rate distributions across the two sets of shapes would have a score of zero and that preference for either the square or the circular enclosure would both have a positive score (see **Figure S4**). For shape preference scores across 16 sessions, chance values were obtained for each CA region by performing random shuffles of shape identity across the 16 recording sessions.

Population Vector Correlations. For each behavioral session and each hippocampal CA region, rate vectors were constructed by arranging the spatial maps of all cells recorded from that region from all animals in an x-y-z stack, where x and y represent the two spatial dimensions and z represents the cell-

identity of tracked cells (Leutgeb et al., 2005a; Leutgeb et al., 2005b). To allow for comparisons between the square and circular enclosure shapes, the analysis was restricted to the 16 by 16 bins that were common to both shapes, yielding 256 x-y locations. Population vector correlations were obtained by calculating, for each x-y location, the Pearson correlation coefficient for firing rates along the z-dimension between pairs of sessions. Cells with firing below 1 Hz in all x-y bins of the two sessions that were compared were excluded from the population vectors before calculating the correlation coefficients. The correlation coefficients of all spatial bins were averaged to estimate the population vector correlation for a pairwise comparison between sessions. For comparisons by time lag within a block, pairs of recording sessions were analyzed based on the number of recording sessions between them (e.g., no intervening session corresponds to lag 1), the experimental paradigm used (two-shape, single-shape), and whether sessions occurred in the same or different shape. Because the sequence of shapes was chosen randomly for each block in the two-shape condition, possible comparisons in a comparison group (e.g., lag 1, same-shape) could include instances in which the shapes were presented at different positions within the recording sequence. For example, same shape comparisons at lag 1 could include instances when the first and second recording session were squares (square 1-square 2), when the second and third recording session were squares (square 2-square 3), or when the third and fourth recording session were squares (square 3-square 4) as well as instances when both of the recordings in a pair were in circles (circle 1-circle 2, circle 2-circle 3, circle 3-circle 4). From each of these possible pairwise comparisons, population vectors were created from cells that were recorded in corresponding shapes over a corresponding lag, and their correlations were included as data points when the vectors consisted of more than 25 cells. Because we only compared lag 1 and lag 2 in the two-shape design, we used Mann-Whitney tests for comparisons that differed by lag. The Holm-Bonferroni method was applied to correct for multiple comparisons. In the single-shape comparisons, three different lags (1, 2, and 3) within a block were compared, and we therefore used a two-way ANOVA by brain region and lag. For comparisons on longer time scales, the population vectors were generated by stacking the cells that were recorded in all animals in each hippocampal subregion in each of the 16 recording sessions. The sessions were sorted by their temporal

order after separating squares and circles. Pairwise comparisons between the 8 stacks in the square and the 8 stacks in the circular enclosure were grouped by time interval between blocks (e.g., 6 hours) and by same/different shape comparison. Population vector correlations were then compared using an ANOVA, with Tukey's Honestly Significant Difference (HSD) criterion for *posthoc* analysis.

Supplemental References

Kempter, R., Leibold, C., Buzsaki, G., Diba, K., and Schmidt, R. (2012). Quantifying circular-linear associations: hippocampal phase precession. J Neurosci Methods 207, 113-124.

Leutgeb, J.K., Leutgeb, S., Moser, M.B., and Moser, E.I. (2007). Pattern separation in the dentate gyrus and CA3 of the hippocampus. Science 315, 961-966.

Leutgeb, J.K., Leutgeb, S., Treves, A., Meyer, R., Barnes, C.A., McNaughton, B.L., Moser, M.B., and Moser, E.I. (2005a). Progressive transformation of hippocampal neuronal representations in "morphed" environments. Neuron 48, 345-358.

Leutgeb, S., Leutgeb, J.K., Barnes, C.A., Moser, E.I., McNaughton, B.L., and Moser, M.B. (2005b). Independent codes for spatial and episodic memory in hippocampal neuronal ensembles. Science 309, 619-623.

Leutgeb, S., Leutgeb, J.K., Treves, A., Moser, M.B., and Moser, E.I. (2004). Distinct ensemble codes in hippocampal areas CA3 and CA1. Science 305, 1295-1298.

Lorente de No, R. (1934). Studies on the structure of the cerebral cortex. II. Continuation of the study of the ammonic system. J Psychol Neural 46, 113-117.

Mankin, E.A., Sparks, F.T., Slayyeh, B., Sutherland, R.J., Leutgeb, S., and Leutgeb, J.K. (2012). Neuronal code for extended time in the hippocampus. Proc Natl Acad Sci U S A 109, 19462-19467.

Mitra, P., and Bokil, H. (2008). Observed Brain Dynamics (Oxford University Press, New York).

Ratzliff, A.D., and Soltesz, I. (2001). Differential immunoreactivity for alpha-actinin-2, an N-methyl-D-aspartate-receptor/actin binding protein, in hippocampal interneurons. Neuroscience 103, 337-349.

Royer, S., Sirota, A., Patel, J., and Buzsaki, G. (2010). Distinct representations and theta dynamics in dorsal and ventral hippocampus. J Neurosci 30, 1777-1787.

Skaggs, W.E., McNaughton, B.L., Gothard, K.M., and Markus, E.J. (1993). An information-theoretic approach to deciphering the hippocampal code. In Advances in Neural Information Processing Systems 5, S.J. Hanson, C.L. Giles, and J.D. Cowan, eds. (San Mateo, CA: Morgan Kaufmann), pp. 1030-1037.

Woodhams, P.L., Celio, M.R., Ulfig, N., and Witter, M.P. (1993). Morphological and functional correlates of borders in the entorhinal cortex and hippocampus. Hippocampus 3 Spec No, 303-311.

Wyszynski, M., Kharazia, V., Shanghvi, R., Rao, A., Beggs, A.H., Craig, A.M., Weinberg, R., and Sheng, M. (1998). Differential regional expression and ultrastructural localization of alpha-actinin-2, a putative NMDA receptor-anchoring protein, in rat brain. J Neurosci 18, 1383-1392.